1 ISASO2 : Recent trends and regional patterns of Ocean Dissolved Oxygen change

2 Nicolas Kolodziejczyk[1], Esther Portela[1], Virginie Thierry[1], Annaig Prigent[1]

3 [1] *Univ. Brest, CNRS, Ifremer, IRD, LOPS laboratory, IUEM, Plouzané, France*

4 *Correspondence to*: Nicolas Kolodziejczyk (nicolas.kolodziejczyk@univ-brest.fr)

5 **Abstract.** Recent estimates of the global inventory of dissolved oxygen (DO) have suggested a decrease of 2% since the
6 1960s. However, due to the sparse historical oxygen data coverage, the DO inventory exhibits large regional uncertainties at
7 interannual timescale. Using ISASO2, a new DO Argo-based optimally interpolated climatology
8 https://doi.org/10.17882/52367(Kolodziejczyk et al.,2021), we have estimated an updated regional oxygen inventory. Over
9 the long term (~1980-2013), comparing the ISASO2 Argo fields with the first guess WOA18 built from the DO bottle
10 samples fields extracted from WOD18, the broad tendency to global ocean deoxygenation remains robust in the upper 2000
11 m with -451±243 Tmol per decade. The oxygen decline is more pronounced in the key ventilation areas of the Southern
12 Ocean and North Atlantic, except in the Nordic Seas, where oxygen has increased. Over the shorter timescale of the Argo
13 period (2005-2019), the deoxygenation tendency seems globally amplified (-1211±218 Tmol per decade). However, DO
14 changes exhibit stronger amplitude and contrasted regional patterns, likely driven by interannual modes of variability in
15 regions as, for instance, the North Atlantic Subpolar-gyre. The recent changes in Apparent Oxygen Utilization mainly
16 explain the interannual variability in the ventilation regions. However, Argo DO coverage is still incomplete at the global
17 and calibration method developpement are still in progress. Continuing the monitoring of the seasonal to interannual and
18 regional to global DO variability from ISASO2 will improve our ability to reduce uncertainties on global and regional DO
19 inventory.

20 1 Introduction

21

22 The global inventory of dissolved oxygen (DO) has been reported to decline about 2% over the last 60 years
23 (Schmidtko et al., 2017 ; Helm et al., 2011 ; Ito et al., 2017). Moreover, future projections suggest a sustained-to-increasing
24 ocean deoxygenation until 2100, depending on the emission's scenario (Bopp et al., 2013). This trend has been partly
25 explained by the loss of solubility due to the warming of the upper ocean layer under global warming of the Earth system
26 (Keeling et al., 2010; Schmidtko et al., 2017). Furthermore, ocean warming and melting of continental ice have
27 consequences on ocean circulation by enhancing surface stratification (Li et al., 2020 ; Yamaguchi & Suga, 2019; Sallée et

28 al., 2021; Bronselaer et al., 2018; IPCC, 2021), which may reduce the ventilation of the DO in the Southern Ocean (Helm et

29 al., 2011; Couespel et al., 2019; Bronselaer et al., 2020), in regions of deep water formation in the northern North Atlantic

30 (Stendardo & Gruber, 2012), and in the shallow thermocline ventilation cells in tropical regions (Oschlies et al., 2018). The

31 latter has particular impact on the weak DO supply to the Oxygen Minimum Zones (OMZs), that are naturally low-oxygen

32 regions located in the eastern tropical oceans (Karstensen et al., 2008 ; Paulmier and Ruiz-Pino, 2009, Hahn et al., 2017).

33 One of the critical manifestations of the global deoxygenation is the expansion of the OMZs (Stramma et al., 2008) with

34 strong impact on the habitat of pelagic species (Stramma et al., 2012) and macrofaunal diversity (Sperling et al., 2016).

35

36 Many efforts have been made recently to gather a comprehensive DO dataset and to diagnose the DO global

37 inventory from historical data sets (e.g. Schmitdko et al., 2017; Helm et al., 2011 ; Ito et al, 2017). However, the interannual

38 and regional DO variability and driving mechanisms, especially those associated to the ocean ventilation (Helm et al., 2011;

39 Portela et al., 2020b), suffer from large uncertainties due to a lack of dedicated and sustained observing systems (Levin,

40 2018; Oshlies et al., 2018). Consequently, at the regional scales, the modes of natural ocean variability need to be better

41 identified, as they can obscure the long-term anthropogenic oxygen trends (e.g. Stramma et al., 2020; Stramma and

42 Schmidtko, 2021; Feucher et al., 2022).

43

44 Since 2005, the development of the BGC-Argo mission collecting biogeochemical parameters such as DO (Claustre

45 et al., 2009; Roemmich et al., 2019) from Argo floats has already provided more than 150,000 quality controlled profiles

46 (Thierry and Bittig, 2021; Maurer et al., 2021). Although still sparse at global scale, the coverage of the Argo DO time series

47 allows resolving the seasonal-to-interannual DO variability at regional scale. In some key regions, such as the North Atlantic

48 subtropical and subpolar gyres, this new dataset has already improved our understanding of the physical drivers of regional

49 DO variability (e.g. Billheimer et al., 2021; Feucher et al., 2022). Thus, sustained and consistent further observations are

50 needed to monitor the oxygen regional and interannual variability and to disentangle the long-term anthropogenic trends

51 from natural variability (Levin et al., 2017). Also, beyond the warming induced ocean deoxygenation, the crucial role of

52 ventilation change in the amplification/attenuation of deoxygenation should be addressed at the regional and interannual

53 timescale.

54

55   In this study, we constructed a climatological gridded product of the most updated Argo DO dataset using the In

56 Situ Analysis System tool (ISAS, Gaillard et al., 2009, 2016). ISAS has been routinely used to optimally interpolate in situ

57 temperature and salinity data, and it has now been adapted for analysis of the Argo DO. The new ISAS climatologies over

58 selected periods between 2005-2019 are compared with the historical World Ocean atlas (WOA18, representative of the

59 early 1980s). The global patterns of the recent DO change over the Argo period (2005-2019) and the long-term variability

60 (1980-2013) are eventually discussed (in regions covered by Argo DO). The climatological ISASO2 fields are freely

61 available at: https://doi.org/10.17882/52367.

62 2 Data and Method

63 2.1 Argo DO data

64   The Argo DO data (2021-03 release) have been downloaded from Coriolis Global Assembly Center (Argo, 2000).

65 In this study, we used 117,359 Delayed Mode (DM) Argo S-profiles from the surface to 2000 m depth covering the period

66 2005-2019 (Fig. 1a). Only Quality Control (QC) flags set to 1 and 2 have been retained by default in the analysis process.

67

68   There are two main methods to measure DO in the ocean from an autonomous platform (Thierry et al. 2022). The

69 first method is an electrochemical method that uses a Clark-type polarographic cell (Gnaigner and Foster, 1983). The SBE43

70 sensor uses this measurement principle. The second method is an optical method based on the principle of dynamic

71 fluorescence quenching (Lakowicz, 2006). Sensors based on this method are referred to as oxygen optodes (e.g. Aanderaa

72 4330, SBE63 and SBE83, AROD-FT Rinko). While the two types of sensors have been tested in the field since 2005, it has

73 been shown that oxygen optodes are the only dissolved oxygen sensors currently suitable for Argo applications (Bittig et al,

74 2019). In addition, sensor models, designs, calibration processes and computing equations have evolved since 2005 (Thierry

75 et al. 2022, Bittig et al., 2018, 2019) with the overall aim to improve DO data accuracy.

76

77   The best accuracy that can be reached with the present sensor type and knowledge is 1-2 µmol kg^{-1} (0,5% O$_2$
78 saturation). This requires the use of optodes with individual multipoint calibration and the adjustment of oxygen data to *in
79 situ* and/or in air reference data (Bittig and Körtzinger,. 2017) to correct for the drift in O$_2$ sensitivity that occurs between
80 calibration and deployment ("storage drift" of order ~5% year^{-1}), as well as the "in situ drift" (order of –0.5% year^{-1}) that
81 occurs during the multiyear deployment period (Bittig et al., 2018, 2019). In addition, oxygen optodes can show a pressure
82 dependent response of the sensor. This pressure has been characterized and is taken into account in the dissolved oxygen
83 computation from the raw data (Bittig et al., 2015, 2018, Thierry et al., 2022). For some floats, an additional pressure
84 correction might be necessary to reach the 1-2 µmol kg^{-1}. It needs to be estimated from ship-based calibrated reference data
85 (Racapé et al. 2019). The last issue concerns a time-dependent lag in response to a change in DO, which affects data
86 accuracy when sensors experience O2 gradients during vertical float displacement. While methods to characterize the
87 response time and to correct for the sensor lag are known (Bittig et al., 2014; Bittig and Körtzinger, 2017; Gordon et al.,
88 2020), they cannot be systematically applied as it requires a timing of each observation, which is not available on all float
89 models. The lack of time response correction can lead to uncertainty of 6-7 µmol kg^{-1} for SBE63 sensor and 13-15 µmol kg^{-1}
90 for Aanderaa 4330 sensor in the most strong oxycline region (Bittig and Kortzinger 2017) and might contribute to the bias of
91 - 1.18 mmol kg^{-1} observed on the float data compared to GLODAP (Sharp et al., 2023).

92

93   The distribution of measurement error provided by Argo DO DMQC reflects the evolution of the sensors and the
94 associated data uncertainties. The measurement errors, as estimated by DMQC operators, are mainly distributed around 2-3
95 µmol kg^{-1}, 7-8 µmol kg^{-1} and 13-14 µmol kg^{-1} (Fig. 2). The former one corresponds to the mean accuracy expected from the
96 current sensor type and knowledge (Thierry and Bittig, 2021, Maurer et al., 2021). The two latter ones mainly reflect the data
97 accuracy of older sensor models, but might be due to specific configurations (deployment in strong oxycline region or lack
98 of reference data). The ISASO2 climatology will be regularly updated, including the updated DMQC S-profiles with the
99 most recent advance in sensor corrections.

100

101   Another source of uncertainty is the inhomogeneous spatio-temporal distribution of the Argo DO data. Data

102 coverage remains sparse in subtropical and tropical regions of the South Atlantic and Indian Ocean, as well as in the eastern

103 subtropical area of the Pacific Ocean (Fig. 1c). The coverage is particularly poor in the Pacific Ocean, while the best sampled

104 regions are the North Atlantic, the Southern Ocean, the Eastern North Pacific and the North Indian Oceans (Fig. 1c).

105

106 **2.2. WOA18 and WOD18 OSD data**

107   The DO annual climatology from WOA18 (Garcia et al., 2019) was used as a first guess for ISASO2 interpolation.

108 WOA18 was constructed by objective analysis (Barnes, 1964) of the available historical Ocean Station Data (OSD) provided

109 within the World Ocean Database, 2018 release (WOD18; Boyer et al., 2019). The OSD WOD18 DO dataset gathers

110 962,219 low vertical resolution profiles over the period 1899-2017, with a strong sampling bias in the Northern Hemisphere

111 (Fig. 1b). The OSD-DO data are obtained from the Winkler titration method, excluding other DO sensor devices (Garcia et

112 al., 2019). The accuracy of the Winker method was established as ±0.3 µmol kg^{-1} (Carpenter, 1965). WOA18 climatology is

113 provided on a 1° grid with an effective horizontal resolution between 892 km and 446 km, and over 102 standard depth

114 levels between the surface and 5500 m depth. As there is no preferred time correlation scale introduced in the WOA18

115 mapping (Garcia et al., 2019), the time representativeness of the WOA18 has been estimated using the OSD profiles

116 distribution of WOD18 (Fig. 1a).

117

118   The bulk of profiles deeper than 1000 m depth was collected mainly over the period 1970-1988 (1st and 3rd quartiles

119 ; Fig. 1a). The spatial distribution of the time representativeness of the WOA18/WOD18 for profiles deeper than at least

120 1000 m depth (Fig. 3d,e) reveals that the median year for the sampling carried out in the Northern Hemisphere ocean falls

121 between 1970-1990 with a variance ranging within 6-20 years. In the Southern Hemisphere the sampling is more recent,

122 between 1980-2000, with the largest spread (up to 25 years) in the South Atlantic Ocean (Fig. 3e). Using these relative

123 time-representativeness values for computing the decadal trends at each grid point, leads to increased uncertainties in the

124 estimate of the median time (see Fig. 3). Over the vertical, the time representativeness of WOA18/WOD18 gives a median

125 time between 1970-1990 in Northern Hemisphere with deeper profile reaching 2000 m depth, while in the Southern

126 Hemisphere the median time is more representative of the 1980-2000 period with larger spreads for samples deeper than

127 1000 m depth (Fig. 4).

128 **2.3 ISAS**

129 Using the In Situ Analysis System tool (ISAS; Gaillard et al. 2009, 2016), an Optimal Interpolation (OI, Bretherton

130 et al., 1976) scheme has been used to map the DO data. The horizontal grid was 0.5° over 187 vertical levels from surface to

131 5500 m depth. The a-priori statistics used in the ISASO2 (ISAS for O2) optimal Interpolation are the DO annual climatology

132 from WOA18 (Garcia et al., 2019) (Fig. 5a), used as a first guess, and updated standard deviations (STD) from Argo DO

133 (binned in 5°x5° boxes ; Fig. 5d). The updated DO STD computed from Argo is representative of the seasonal to interannual

134 variance. In comparison to WOA variance climatology, new Argo DO data have significantly improved the a priori

135 estimation of the DO variance in regions historically ill-sampled, such as the Southern Hemisphere (see Fig. 5b,d). New

136 regions of high DO variability have been identified, such as in the western boundary currents and the Antarctic Circumpolar

137 Current. These regions are associated with frontal regions with sharp contrasts between water masses and strong dynamical

138 features that likely produce high DO variability (e.g. Chapman et al., 2020).

139

140 The Argo DO sampling coverage is not yet evenly distributed over the global ocean. Therefore, to deal with the

141 partial coverage, the objective mapping was first performed for the mean state over three selected multiyear periods. In order

142 to be consistent with the spatial scale of ISAS20 temperature and salinity fields also used in this study (Kolodziejczyk et al.,

143 2021), the zonal and meridional decorrelation radius and variance weights are the same as in Gaillard et al. (2016; their

144 equation 4), except for the correlation timescale, the time correlation Gaussian function, defined as:

145 $$C(dt) = \sigma exp\left(\frac{dt^2}{2L_t^2}\right) (1),$$

146

147 where L_t is the time decorrelation scale. The three configurations are: i) ISASO2_MEAN that maps the whole Argo data set

148 using a time correlation Gaussian window centered on January 2013 with a five-year correlation scale (half Gaussian width

149 is L_t = 5 years). This mean encompasses 10 years of data and is designed to be representative of the decadal mean over the

150 period 2009-2018. ii) ISASO2_M11 and ISASO2_M16 are pentadal means using a time correlation Gaussian window

151 centered on January 2011 and 2016, respectively, with a 2.5 years correlation scale (encompassing five years of data). These

152 two configurations are designed to be representative of the ocean's pentadal mean over the periods between 2009-2013 and

153 2014-2018, respectively. This approach was chosen for being a trade-off between having sufficient spatial coverage and

154 allowing a temporal discretization.

155

156   In addition, the DO concentration at saturation $[O_2^{sat}]$ has been computed using the ISAS20 T/S monthly fields

157 averaged over the same three periods (Kolodziejczyk et al., 2021). The DO and Apparent Oxygen Utilisation (defined as

158 AOU= $[O_2^{sat}]$-$[O_2]$) mean climatology have been provided by the World Ocean Atlas 2018 (WOA18, Garcia et al., 2019).

159

160   It is worth addressing the innovation of the DO Argo profiles using WOA18 first guess in the OI ISASO2

161 procedure. Clearly, the time representativeness of both datasets is different. The distribution of the difference between DO

162 Argo observations and WOA18 first guess at the location of the DO Argo profiles shows an average shift of -4.31 µmol.kg^{-1}

163 (Fig. 6). This suggests a general deoxygenated bias between the WOA18 and Argo data likely due to either i) a mean

164 deoxygenation at the location of the DO Argo profile, or ii) remaining low oxygen bias in DO Argo profiles. In contrast,

165 after the OI procedure, the median of residuals, i.e. the difference between DO Argo observations and ISASO2_MEAN at

166 the location of the DO Argo profiles, is -0.39 µmol.kg^{-1} (Fig. 6). This suggests that ISASO2_MEAN estimates are slightly

167 more oxygenated than DO Argo data at the location of the DO Argo profiles. More generally, the DO ISASO2_MEAN

168 slightly overestimates the DO in the period 2005-2019. This is likely due to the relaxation of the DO estimates towards the

169 first guess (WOA18) which is typically less oxygenated, and the smoothing in the ISAS OI procedure.

170

171 **2.2. Error handling**

172

173   The analyzed variance (error) is provided from the OI procedure. It is derived from the a priori variance updated

174 from new Argo DO (Fig. 1c), covariance scales and measurement error (Fig. 2) (Gaillard et al., 2009, 2016). Then, the error

175 estimates of the regional DO inventory is computed by propagating the analyzed error computed from ISASO2 (Fig. 5d),

176 using the linear expression:

177
$$\sigma^2 = \sum_i^N \alpha_i \sigma_i + \sum_i^N \sum_{j \neq i}^N \alpha_i \alpha_j \sigma_i \sigma_j \rho_{ij} \quad (1)$$

178 where α_i is an element of space (layer thickness multiplied by the mean density for vertical inventory or grid cell surface for

179 global inventory), ϵ_i the error at the i grid point, and ρ_{ij} is the correlation between the i and j grid points. This equation was

180 applied for vertical and horizontal summation of error. Correlation ρ_{ij} was computed from ISAS20 monthly temperature

181 fields, assuming that large physical correlation scales can be applied to DO profiles. For computing the WOA18 DO

182 inventory error, the a priori variance is inaccurate and an analyzed error is not provided. Therefore, the full a priory variance

183 derived from Argo DO was used. This should be considered as an upper bound of the WOA18 DO inventory.

184

185   The error on a zonal average section is computed for each section cell using Smith et al. (1994) expression for

186 averaging spatial error :

187
$$\epsilon^2 = \frac{\overline{\epsilon_i^2}}{Dof} \quad (2)$$

188 where, ϵ_i^2 is the quadratic average of the individual analyzed error along a zonal band; and *Dof* is the degree of freedom

189 corresponding to the number of independent grid cells, *i.e.* the total number of grid cells divided by the number of grid cell

190 corresponding to the largest correlation scale used in ISAS (Gaillard et al. , 2016; von Schukmann et al., 2009).

191 **2.3. Computation of trends**

192   The computation of the decadal (pseudo)trend of the DO inventory or concentration is :

193 $$\Delta O_2^{trend} = 10 \times \frac{O_2^{clim1} - O_2^{clim2}}{T_1 - T_2} \quad (2)$$

194   where O_2^{Clim1} and O_2^{clim2} are the DO inventory maps or concentration sections computed from two distinct means

195 and T_1, T_2 are their respective median time. In the case of the three ISASO2 means, this is the central time of the analysis. In

196 the case of the WOA, we have taken the representative time estimated using the median time distribution of the WOD18

197 OSD profiles (Fig. 3d,e). In both cases, we computed decadal trends, even if the difference between ISASO2 means is

198 representative of only a five-year variability. This choice has been made to make comparable (normalize) the magnitude of

199 the long-term and interannual variability. The associated uncertainty ranges for DO inventory and concentration trends have

200 been estimated using propagation techniques of the analyzed error of ISASO2 (detailed in Supplementary Information). The

201 calibration biases may affect the long-term trends. Introducing artificial bias correction (around 1 µmol.kg^{-1}) does not change

202 the regional pattern of DO increase/reduction (not shown). However, mean bias smaller than -1 µmol.kg^{-1} could dramatically

203 impact the total global inventory long-term trend, as our calculation method would overweight the Argo data in the

204 comparison with WOA climatology.

205

206   Three climatological configurations representative of 3 different periods are used to compute DO change, named i)

207 ISASO2_MEAN minus WOA18, which corresponds on average to the period Argo (2009-2018) minus pre-Argo and ii)

208 ISASO2_M16 minus ISASO2_M11, which corresponds to the period 2018-2014 minus 2013-2009 (five-year average). The

209 differences are normalized using the time span between WOA18/WOD18 local median year (Fig. 3d and 4) and 2013

210 (central time of ISASO2_MEAN), and between 2016-2011 (5 years), respectively. The computed trend is normalized in

211 terms of equivalent trend in µmol kg^{-1} or Tmol per decade. For both periods, the error is computed by propagating the error

212 as follows :

213 $$\epsilon \approx \left| \frac{x_i^a - x_j^a}{T} \right| \sqrt{\frac{\epsilon_i^2 + \epsilon_j^2}{\left(x_i^a - x_j^a\right)^2} + \frac{\epsilon_T^2}{T^2} + cov} \quad (3)$$

214 where, $x^a_{i,j}$ are the analyzed fields with i,j in WOA, ISASO2_MEAN, ISASO2_M11, and ISASO2_M16 , T is the median

215 time span between two compared analyzes i,j or estimated by WOD18 profiles median time in the case of using WOA18 (see

216 map Fig. 1c) , $\epsilon_{i,j}$ error of analysis, ϵ_T the variance of the median time span between analysis i,j (map Fig. 3d), *cov* is the

217 covariance between different errors which is assumed to be zero. For the WOA18 as no analysis error is provided, we have

218 taken STD computed from DO Argo (Fig. 5d). This estimate is likely an upper bound of the errors of analysis (corresponding

219 to a percentage of variance (PCTVAR) of 100% in the OI).

220

221   In order to assess the robustness of our approach to estimate the change in DO, we have computed the DO trends in

222 5°x5° boxes using a linear regression of individual profiles at 500 (not shown) and 1000 m depth (± 50 m) using OSD plus

223 Argo data (Fig. 7c), WOD18 alone (Fig. 7d), and Argo data alone (Fig. 7e). Three features can be highlighted from this

224 analysis: (i) the comparison with computation of equivalent trends from OSD and ISAS interpolated fields provides the same

225 order of magnitudes and comparable regional pattern of trends (Fig. 7a,b,c,e). (ii) The most striking features are the larger

226 magnitudes of the trends (in absolute value) during the Argo period, reaching more than twice those of the pre-Argo period.

227 (iii), using the OSD dataset alone over the pre-Argo period (Fig. 7d) provides inconsistent trends (compared to Argo+OSD,

228 Fig. 7c) in ill-sampled regions such as the Southern Ocean, and generally non-significant trends due to lack of data in many

229 other regions (Fig. 7d).

230

231   In order to get further confidence in the mapped trends, we have also computed DO trends at selected locations over

232 the global ocean (Fig. 8). In historically ill-sampled regions, such as the Southern Ocean, Subtropical and mid-latitude

233 regions, trends are generally barely significant and not consistent among dataset (Fig. 7 and 8a,d,e). In these cases, Argo

234 floats provide data over the recent period that allowed to better constrain the long term trend. In contrast, well sampled

235 regions, such as North Atlantic, North Pacific and, Nordic Seas and, exhibit robust long-term trends (Fig. 7-8b,c,f).

3 Results

The updated global DO inventory computed from ISASO2_MEAN gives about 235.2±0.1 Pmol (236±0.1 Pmol for WOA18O2), which is close to the 227.4±1.1 Pmol computed from Schmidko et al. (2017) with a different data set and mapping method. The ~1980-2013 global DO inventory change given by ISASO2_MEAN minus WOA18 is around -451±243 Tmol per decade for the upper 2000 m depth.

The global map of DO inventory change depicted in Figure 9a, reflects the regional mean equivalent trends between the Argo and pre-Argo period. The global ocean has generally deoxygenated over several decades, except in the Nordic Seas (+ 4 mol.m^{-2} per decade) and in few regions of the Subtropical Southern Indo-Pacific (> +10 mol.m^{-2} per decade; Fig. 9a). The Northern Atlantic and Pacific Ocean are deoxygenating at a rate around -6 mol.m^{-2} per decade, and the tropical OMZs in the majority of the basins have expanded at 1000 m depth (black and red contours, Fig. 9a). The addition of new DO Argo data in this study has provided more robust patterns in the mid-latitude Southern Ocean in regions were Argo floats have been deployed (Fig. 9a). The Southern Ocean has been historically poorly sampled in terms of DO, thus its contribution to global deoxygenation since 1980 (about 42%) might have been underestimated or impossible in previous studies (Ito et al., 2017). This DO loss is comparable to that of the Tropical band over the same period (43% between 30°S-N).

The DO Argo data provide further insight on the interannual changes of the DO inventory over the last 10 years (Fig. 9b). Globally, the ocean has lost the equivalent of about -1211±218 Tmol of DO per decade over the Argo period (deduced from ISASO2_16 minus ISASO2_11). This suggests a much more intense interannual variability in comparison to the longer-term change previously reported in the literature and in this study (e.g Schmidtko et al., 2017). Furthermore, over the Argo period, the regional patterns are more than twice as intense as the regional patterns of the long term trends, but in line with regional change due to natural mode of variability (e.g. Stramma and Schmidtko, 2021; Fig. 9ab). The North Atlantic Subpolar Gyre, the Nordic Sea, and the Gulf Stream regions show the largest spatially coherent increase of DO inventory (> + 20 mol.m^{-2} per decade, Fig. 9b). In contrast to the long-term trends, the Southern Ocean around 35-50°S (i.e.

260 subtropical front) exhibits a more intense increase of DO inventory (> + 10 mol.m^{-2} per decade) while, south of 50°N, more

261 intense deoxygenation dominates (< -15 mol.m^{-2} per decade).

262

263   The processes generally invoked to explain the global deoxygenation are the decrease in seawater

264 solubility ([O2^{sat}]) directly induced by the ocean warming, and reduced ocean ventilation combined with increased biological

265 utilization. These last two processes reflect an increase of the AOU (a proxy of the water-mass age). Zonally averaged

266 sections of DO concentration, [O2^{sat}] and AOU as well as their temporal changes are used to better illustrate and understand

267 interannual and long term DO variability and their driving mechanisms (Fig. 10 and Fig. 11-14). Long-term regional

268 deoxygenation (Fig 10d) occurs mainly in the Southern Ocean and Northern Hemisphere, in the upper 1500 m, except in the

269 subpolar northern latitudes (45-60°N) where it reaches down to 2000 m depth (not enough deeper DO Argo data are

270 available; Fig. 10ad) with an average trend of around 2 µmol.kg^{-1} per decade. This is mainly explained by deoxygenation in

271 NADW in the Atlantic basin (Fig. 11ad). In contrast, the water column in the Nordic Seas (>60°N) has oxygenated, mainly

272 below 1000 m depth (Fig. 10d and 11d). The Southern Ocean has generally deoxygenated between the lower Antarctic

273 Intermediate Waters and the Upper Circumpolar Deep Waters (σ_θ~27.2-27.8 kg.m^{-3}, ~2 µmol.m^{-2} per decade, Fig. 10a,d). In

274 contrast, deepening of the isopycnals of the well ventilated SubAntarctic Mode Water (SAMW), indicates a volume increase

275 of the water masses, although with no significant DO increase (Fig. 10a,d). Between 20°S-20°N, the tropical band exhibits

276 slight deoxygenation in the upper 1000 m (1 µmol.kg^{-1} per decade). The tropical and equatorial deoxygenation, mainly

277 observed in the east of the Atlantic and Pacific and northern Indian basins, is consistent with the observed decadal increase

278 of the OMZs volume (Stramma et al., 2008; Fig. 10a,b and Fig. 11-13a,d).

279

280   The observed last-decade change reveals that the interannual-to-decadal variability can be twice as large as the long

281 term trend in some specific regions (Fig. 11). As an exception, over the Argo period, the Northern Hemisphere north of 40°N

282 exhibits an oxygenation signal (>5 µmol.m^{-2} per decade Fig. 10g) that opposes the long-term mean, especially in the North

283 Atlantic Subpolar gyre, down to 1500 m depth (>10 µmol.kg^{-1} per decade, Fig. 11g). In the Southern Hemisphere there are

284 differences between ocean basins. In the Indo-Pacific basins (Fig. 12g and 13g), over the Argo period, the deoxygenation is

285 more intense and deeper than in the pre-Argo period. Particularly, the DO loss within the Upper Circumpolar Deep Water

286 (around σ_θ=27.5 kg.m^{-3}) exceeds 8 µmol.kg^{-1} per decade (Fig. 10g and Fig 11-14g). In contrast, the Atlantic basin exhibits a

287 smaller oxygen loss or even oxygen gain over the upper 1000 m, and a slightly more intense deoxygenation between 1000m

288 and 2000 m (Fig 11d,g).

289

290 Over the recent (long-term) period, solubility contributed to ~30% (50%) of the global deoxygenation in the upper

291 2000 m of the water column (Fig.10e,h). Over both periods, the regional (de)oxygenation appears to be mainly driven by

292 AOU-related processes (Fig. 10f,i and 12-14f,i). AOU changes are also dominant over the shorter time scales, as they

293 explain the DO change patterns in most regions and depth ranges (Fig. 10i and 12-14i). Although it is complex to disentangle

294 the physical ventilation from biological consumption in AOU changes, four main patterns show up from the Figure 10f,i

295 (and Fig. 11-14f,i) : i) AOU Increase in the Southern Ocean below the Intermediate Waters ($\sigma_\theta \geq$27.5 kg.m^{-3}); ii) AOU

296 Increase within the tropical band of the three oceanic basins (Fig. 10f,i and 11-14f,i); iii) AOU increase (decrease) of the

297 surface to subsurface waters over the long-term period (Argo period) in the North Atlantic Subpolar gyre and North Pacific

298 (Fig. 11,12f,i); and iv) AOU decrease North of 70°N in the Nordic Seas around 1000 m depth (Fig. 11f).

299 **DataAvailability** : Data described in this manuscript can be accessed at SEANOE under https://doi.org/10.17882/52367

300 (Kolodziejczyk et al., 2021)

4 Discussion and Conclusion

301

302   The updated ISASO2 climatologies, with DMQC DO Argo profiles, provide new insight on the recent change in

303 global and regional patterns of DO in the context of the global ocean deoxygenation. First, comparing the ISASO2 Argo

304 fields with the WOA18 built from the DO bottle samples fields extracted from WOD18, i.e. the most reliable historical

305 dataset, the broad tendency to global ocean deoxygenation remains robust in the upper 2000 m with -451±243 Tmol per

306 decade between 1980-2013. In spite of a large range of values and no common time and space coverage over the estimated

307 values, our results are in line with previous studies. Using WOCE data, Helm et al. (2012) found -550±25 Tmol per decade

308 within 100-1000 m depth surface layer between 1970-1990 ; Schmidko et al., (2017) found a trend of -961 ± 429 Tmol per

309 decade in the full water column between 1960-2015; and Ito et al. (2017) reported DO trends of -243±124 Tmol per decade

310 in the upper 1000 m depth between 1958-2015. In spite of different methods in estimating the uncertainty among the

311 literature, the relative magnitude of uncertainty estimate on global trends is also generally in line with previous studies.

312

313   Although DO Argo coverage is still partial in some regions, some contrasted regional patterns between the

314 pre-Argo and Argo periods are emerging from the updated dataset. For instance, the historically ill-sampled Southern Ocean

315 shows clear deoxygenation over at least the last two decades. Moreover, consistent sampling over the Argo period has

316 allowed us to provide pentadal to decadal mean for these regions. Although the deoxygenation tendency seems globally

317 amplified (-1211±218 Tmol per decade), we cannot argue an acceleration of deoxygenation over the Argo period. Rather, the

318 global inventory may be sensitive to very large regional and interannual variability, as suggested by our map and sections of

319 interannual change. As reported in recent studies (Stramma et al., 2020; Stramma and Schmitdko, 2021, Feucher et al.,

320 2022), natural modes of variability are known to strongly impact the ocean DO change at regional scale. The Argo DO

321 standard deviation and trends estimates shown here, reveal for the first time the very inhomogeneous and intense DO

322 variability over the ocean. This may help to quantify the range of uncertainty induced by natural/interannual variability over

323 the longer-term deoxygenation trends. For instance, the North Atlantic Subpolar gyre exhibits a recent oxygenation,

324 explained by AOU decrease due to the intensification and cooling of the subpolar gyre and the return of deep convection

325 favouring the sequestration of DO in the intermediate Labrador Sea Water, as reported in the Irminger Sea (Tjiputra et al.,

326 2018, Feucher et al., 2022). In this region, the interannual to decadal variability of ventilation makes it difficult to observe a

327 significant long-term deoxygenation trend (Feucher et al., 2022).

328

329   Noticeable oxygenation patterns are observed in the deep Nordic Seas, especially north of 70°N in the Greenland

330 Sea. Since the late 90's, deeper convection has been reported in the Greenland Sea (1500 m depth) while the temperature of

331 intermediate water has increased (Brakstad et al., 2019). The latter is compatible with observed continuous decrease in

332 oxygen solubility. However, deeper convection contributes to replenish DO at depth, making the intermediate water younger

333 (decreasing AOU) and then, overcoming the solubility decrease (Lauvset et al., 2018). Interestingly, besides the strong

334 interannual variability, the long-term DO decline in North Atlantic, both in Labrador Sea Water and NADW, as well as DO

335 increase in the deep Greenland Sea, suggest a northward shift of the DO ventilation. In climate model future projections, a

336 warmer and more stratified ocean suggest a northward shift of the AMOC ventilation hot-spots as the winter sea-ice

337 maximum extension retreats (Lique & Thomas, 2018).

338

339   The Southern Ocean, which has been historically less consistently sampled, also reveals the large deoxygenation

340 that has been reported near the Antarctic continent. The input of meltwater in Antarctica, and poleward wind shift in the

341 Southern Ocean have been suspected to be responsible for increasing stratification. The latter would reduce ventilation and

342 water-mass age (AOU) near the continent and within the Circumpolar Deep Water with a potential strong impact on

343 biological productivity (Bronsealer et al., 2016, 2018). Interestingly, SAMW that is a hot-spot of DO ventilation (Portela et

344 al., 2020b) does not show any significant change over the long term in spite of their volume increase during the last decades

345 (Kolodziejczyk et al., 2019, Portela et al, 2020a). In contrast, over the Argo period, strong variability of

346 deoxygenation/oxygenation patterns is reported around the Southern Ocean, with oxygenation of the mode/intermediate

347 waters during the last decade and deoxygenation of Circumpolar Deep Water. In the latter case, wind and isopycnal mixing

348 change (Abernathy and Ferreira, 2015; Naveira-Garabato et al., 2017), as well as stronger stratification (Bronsealer et al.,

349 2018) have been suggested to play a key role in modulating tracer ventilation in the Southern Ocean (Morrison et al., 2022).

15

350 The precise role of long-term increased stratification and/or change in isopycnal mixing, as well as the recent Southern

351 Ocean deoxygenation should be addressed in future studies.

352

353 Our study is mainly based on the historical bottle samples (OSD WOA18) and the recent DO Argo dataset

354 (ISASO2). Excluding other oxygen profiles over the historical period may cause less resolved historical time series and

355 spatial coverage, especially in the poorly sampled regions like the Southern Ocean. This may increase the uncertainties on

356 trends computation: as it is well known, the lack of data coverage may result in underestimating the global trends computed

357 from parameters analyzed with optimal interpolation methods (Lymann and Johnson, 2011). However, continuous sampling

358 of the Argo network helps to remove the seasonal bias usually associated with the historical cruises mainly occurring during

359 summer. It also allows better estimates of the DO natural seasonal-to-interannual STD which is crucial for computing the

360 range of uncertainties (Fig. S1d), even if the DO eddy variance contribution is still to be estimated (Atkins et al., 2022).

361

362 A major source of uncertainty on DO Argo data in this study is the calibration of the DO profiles, which can exhibit

363 remaining low oxygen bias larger than 1 to 3 $\mu mol.kg^{-1}$ that could be due to uncorrected sensor time response (Bittig et al.,

364 2014 ; Maurer et al., 2021, Sharp et al., 2023). Continuous monitoring and progress in Argo DO time response and drift

365 correction is mandatory to ensure quality and consistency among the DO dataset of different origins. Regarding the historical

366 OSD data, the accuracy of the Winkler titration method is generally ± 0.3 $\mu mol\ kg^{-1}$ (Carpenter, 1965). However, larger

367 uncertainties are expected due to change of the sampling and titration methods over the last century. Nevertheless, the still

368 sparse DO data is probably the main source of uncertainties, especially when using the ISAS_M11 and ISAS_M16

369 configurations that present the most limited Argo coverage of the 5-years windows. Also, we hope that the ongoing

370 deployment of global Argo DO observations will help to update the ISASO2 analysis in order to provide DO global fields

371 with better spatial coverage and enhanced time discretization.

372

373 Therefore, long-term observations and consistent spatial coverage of the ocean DO, combined with other BGC

374 parameters in the framework of OneArgo will provide further insight on the regional mechanisms of ocean deoxygenation.

375 Moreover, this can finally shed some light on their still poorly known oxygen biological drivers (Levin et al., 2017; Oschlies

376 et al., 2018).

377 **Competing interests :** The contact author has declared that none of the authors has any competing interests.

385 **Open Research** : Argo data are freely available at Argo (2000). ISAS T/S/O2 fields are freely available at Kolodziejczyk et

386 al. (2021). WOA18 fields and WOD18 are freely available at Boyer et al., (2018) and Boyer et al. (2016) , respectively.

Open Access

Earth System **Science** **Data** Discussions

References:

388 Abernathey, R., and D. Ferreira (2015), Southern Ocean isopycnal mixing and ventilation changes driven by winds,
389   Geophys. Res. Lett., 42, 10,357–10,365, doi:10.1002/2015GL066238.

390 Argo (2000): Argo float data and metadata from Global Data Assembly Centre (Argo GDAC).
391   SEANOE. https://doi.org/10.17882/42182.

392 Atkins, J., Andrews, O., & Frenger, I. (2022). Quantifying the Contribution of Ocean Mesoscale Eddies to Low Oxygen
393   Extreme Events. *Geophysical Research Letters*, *49*(15).[dataset] https://doi.org/10.1029/2022GL098672

394 Billheimer, J., S., Talley, L. D., & Martz, T. R. (2021). Oxygen Seasonality, Utilization Rate, and Impacts of Vertical
395   Mixing in the Eighteen Degree Water Region of the Sargasso Sea as Observed by Profiling Biogeochemical
396   Floats. *Global Biogeochemical Cycles*, *35*(3), 1–19. https://doi.org/10.1029/2020GB006824

397 Bittig, Henry C., Fiedler, Björn, Scholz, Roland, Krahmann, Gerd, Körtzinger, Arne, (2014), Time response of oxygen
398   optodes on profiling platforms and its dependence on flow speed and temperature, *Limnology and Oceanography:*
399   *Methods*, 12, doi: 10.4319/lom.2014.12.617.

400 Bittig, H. C. and Körtzinger, A. (2017): Technical note: Update on response times, in-air measurements, and in situ drift
401   for oxygen optodes on profiling platforms, Ocean Sci., 13, 1–11, https://doi.org/10.5194/os-13-1-2017.

402 Bittig, H. C., Körtzinger, A., Neill, C., van Ooijen, E., Plant, J. N., Hahn, J., et al. (2018). Oxygen optode sensors:
403   principle, characterization, calibration, and application in the ocean. Front. Mar. Sci. 4:429. doi:
404   10.3389/fmars.2017.00429

405 Bittig, H.,Maurer, T., Plant, J., Schmechtig, C., Wong, A., Claustre, H., et al. (2019). A BGC-argo guide: planning,
406   deployment, data handling and usage. Front.Mar. Sci. 6:502. doi: 10.3389/fmars.2019.00502

407 Bopp, L., Resplandy, L., Orr, J. C., Doney, S. C., Dunne, J. P., Gehlen, M., Halloran, P., Heinze, C., Ilyina, T., Séférian,
408   R., Tjiputra, J., & Vichi, M. (2013). Multiple stressors of ocean ecosystems in the 21st century: Projections with
409   CMIP5 models. *Biogeosciences*, *10*(10), 6225–6245. https://doi.org/10.5194/bg-10-6225-2013

410 Boyer, Tim P.; Garcia, Hernan E.; Locarnini, Ricardo A.; Zweng, Melissa M.; Mishonov, Alexey V.; Reagan, James R.;
411   Weathers, Katharine A.; Baranova, Olga K.; Seidov, Dan; Smolyar, Igor V. (2018). World Ocean Atlas 2018.
412   [indicate subset used]. NOAA National Centers for Environmental Information. [Dataset].
413   https://www.ncei.noaa.gov/archive/accession/NCEI-WOA18. Accessed 2022

414 Boyer, Tim P.; Antonov, John I.; Baranova, Olga K.; Coleman, Carla; García, Hernán E.; Grodsky, Alexandra; Johnson,
415   Daphne R.; Locarnini, Ricardo A.; Mishonov, Alexey V.; O'Brien, Todd D.; Paver, Christopher R.; Reagan, James
416   R.; Seidov, Dan; Smolyar, Igor V.; Zweng, Melissa M. (2016). NCEI Standard Product: World Ocean Database
417   (WOD). [indicate subset used]. NOAA National Centers for Environmental Information. [Dataset].
418   https://www.ncei.noaa.gov/archive/accession/NCEI-WOD. Accessed 2022.

419 Brakstad, A., Våge, K., Håvik, L., & MOORE, G. W. K. (2019). Water mass transformation in the Greenland sea during
420   the period 1986-2016. *Journal of Physical Oceanography*, *49*(1), 121–140.
421   https://doi.org/10.1175/JPO-D-17-0273.1

422 Bronselaer, B., Russell, J. L., Winton, M., Williams, N. L., Key, R. M., Dunne, J. P., Feely, R. A., Johnson, K. S., &
423   Sarmiento, J. L. (2020). Importance of wind and meltwater for observed chemical and physical changes in the
424   Southern Ocean. *Nature Geoscience*, *13*(1), 35–42. https://doi.org/10.1038/s41561-019-0502-8

425 Bronselaer, B., Winton, M., Griffies, S. M., Hurlin, W. J., Rodgers, K. B., Sergienko, O. V., Stouffer, R. J., & Russell, J.
426   L. (2018). Change in future climate due to Antarctic meltwater. *Nature*, *564*(7734), 53–58.
427   https://doi.org/10.1038/s41586-018-0712-z

428 Carpenter, J.H. (1965). The Chesapeake Bay Institute technique for the Winkler dissolved oxygen titration, Limnol.
429   Oceanogr., 10, 141-143.

430 Chapman, C.C., Lea, MA., Meyer, A. *et al.* Defining Southern Ocean fronts and their influence on biological and
431   physical processes in a changing climate. *Nat. Clim. Chang.* **10**, 209–219 (2020).
432   https://doi.org/10.1038/s41558-020-0705-4.

433 Couespel, D., Lévy, M., & Bopp, L. (2019). Major Contribution of Reduced Upper Ocean Oxygen Mixing to Global
434   Ocean Deoxygenation in an Earth System Model. *Geophysical Research Letters*, *46*(21), 12239–12249.
435   https://doi.org/10.1029/2019GL084162

436 Feucher, C., Portela, E., Kolodziejczyk, N., & Thierry, V. (2022). Subpolar gyre decadal variability explains the recent
437   oxygenation in the Irminger Sea. *Communications Earth & Environment*, *3*(1), 1–9.
438   https://doi.org/10.1038/s43247-022-00570-y

439 Gnaigner, E., and H. Forstner, Ed., 1983: Polarographic Oxygen Sensors: Aquatic and Physiological Applications,
440   Springer-Verlag, 370 pp.

441 Gaillard, F., E. Autret, V. Thierry, P. Galaup, C. Coatanoan, and T. Loubrieu, (2009): Quality Control of Large Argo
442   Datasets. *J. Atmos. Oceanic Technol.*, **26**, 337–351, https://doi.org/10.1175/2008JTECHO552.1.

443 Gaillard, F., Reynaud, T., Thierry, V., Kolodziejczyk, N., & Von Schuckmann, K. (2016). In situ-based reanalysis of the
444   global ocean temperature and salinity with ISAS: Variability of the heat content and steric height. *Journal of*
445   *Climate*, *29*(4), 1305–1323. https://doi.org/10.1175/JCLI-D-15-0028.1

446 Garabato, A. C. N., MacGilchrist, G. A., Brown, P. J., Evans, D. G., Meijers, A. J. S., & Zika, J. D. (2017).
447   High-latitude ocean ventilation and its role in Earth's climate transitions. *Philosophical Transactions of the Royal*
448   *Society A: Mathematical, Physical and Engineering Sciences*, *375*(2102). https://doi.org/10.1098/rsta.2016.0324

449 Garcia, H. E., K. Weathers, C. R. Paver, I. Smolyar, T. P. Boyer, R. A. Locarnini, M. M. Zweng, A. V. Mishonov, O. K.
450   Baranova, D. Seidov, and J. R. Reagan, 2018. World Ocean Atlas 2018, Volume 3: Dissolved Oxygen, Apparent
451   Oxygen Utilization, and Oxygen Saturation. A. Mishonov Technical Ed.; NOAA Atlas NESDIS 83, 38pp.

452 Gordon, C., Fennel, K., Richards, C., Shay, L. K., and Brewster, J. K. (2020). Can ocean community production and
453   respiration be determined by measuring high-frequency oxygen profiles from autonomous floats? Biogeosciences
454   17, 4119–4134. doi: 10.5194/bg-17-4119-2020
455
456 Hahn, J., Brandt, P., Schmidtko, S., & Krahmann, G. (2017). Decadal oxygen change in the eastern tropical North
457   Atlantic. *Ocean Science*, *13*(4), 551–576. https://doi.org/10.5194/os-13-551-2017
458 Helm, K. P., Bindoff, N. L., & Church, J. A. (2011). Observed decreases in oxygen content of the global ocean.
459   *Geophysical Research Letters*, *38*(23), 1–6. https://doi.org/10.1029/2011GL049513
460 Ito, T., Minobe, S., Long, M. C., & Deutsch, C. (2017). Upper Ocean O$_2$ trends: 1955-2015. *Geophy. Res. Lett.*,
461   4214–4223. https://doi.org/10.1002/2017GL073613
462 Karstensen, J., Stramma, L., & Visbeck, M. (2008). Oxygen minimum zones in the eastern tropical Atlantic and Pacific
463   oceans. *Progress in Oceanography*, *77*(4), 331–350. https://doi.org/10.1016/j.pocean.2007.05.009
464 Keeling, R. F., Körtzinger, A., & Gruber, N. (2010). Ocean deoxygenation in a warming world. *Annual Review of*
465   *Marine Science*, *2*(1), 199–229. https://doi.org/10.1146/annurev.marine.010908.163855
466 Kolodziejczyk N., Prigent-Mazella A., Gaillard F. (2021). ISAS temperature and salinity gridded fields. SEANOE.
467   [dataset]. https://doi.org/10.17882/52367
468 Kolodziejczyk, N., Llovel, W., & Portela, E. (2019). Interannual variability of upper ocean water masses as inferred
469   from Argo Array. Journal of Geophysical Research: Oceans, 124. https://doi.org/10.1029/2018JC014866
470 Lauvset, S. K., Brakstad, A., Våge, K., Olsen, A., Jeansson, E., & Mork, K. A. (2018). Continued warming,
471   salinification and oxygenation of the Greenland Sea gyre. *Tellus, Series A: Dynamic Meteorology and*
472   *Oceanography*, *70*(1), 1–9. https://doi.org/10.1080/16000870.2018.1476434
473 Levin, L. A. (2018). Manifestation, drivers, and emergence of open ocean deoxygenation. *Annual Review of Marine*
474   *Science*, *10*, 229–260. https://doi.org/10.1146/annurev-marine-121916-063359
475 Li, G., Cheng, L., Zhu, J., Trenberth, K. E., Mann, M. E., & Abraham, J. P. (2020). Increasing ocean stratification over
476   the past half-century. *Nature Climate Change*, *10*(12), 1116–1123. https://doi.org/10.1038/s41558-020-00918-2
477 Lique, C., & Thomas, M. D. (2018). Latitudinal shift of the Atlantic Meridional Overturning Circulation source regions
478   under a warming climate. *Nature Climate Change*, *8*(11), 1013–1020. https://doi.org/10.1038/s41558-018-0316-5
479 Maurer, T.L., Plant J.N. and Johnson KS (2021) Delayed-Mode Quality Control of Oxygen, Nitrate, and pH Data on
480   SOCCOM Biogeochemical Profiling Floats. Front. Mar. Sci. 8:683207. doi: 10.3389/fmars.2021.683207
481 Morrison, A. D. Darryn W. Waugh, Andrew McC. Hogg, Daniel C. Jones, Ryan P. Abernathey, Ventilation of the
482   Southern Ocean Pycnocline, Annual Review of Marine Science 2022 14:1, 405-430

483 Naveira Garabato AC, MacGilchrist GA, Brown PJ, Evans DG, Meijers AJS, Zika JD. 2017 High-latitude ocean
484   ventilation and its role in Earth's climate transitions. Phil.Trans.R.Soc.A 375: 20160324.
485   http://dx.doi.org/10.1098/rsta.2016.0324

486 Oschlies, A., Brandt, P., Stramma, L., & Schmidtko, S. (2018). Drivers and mechanisms of ocean deoxygenation.
487   *Nature Geoscience*, *11*(7), 467–473. https://doi.org/10.1038/s41561-018-0152-2

488 Portela, E., Kolodziejczyk, N., Vic, C., & Thierry, V. (2020). Physical Mechanisms Driving Oxygen Subduction in the
489   Global Ocean. *Geophysical Research Letters*, *47*(17), 1–10. https://doi.org/10.1029/2020GL089040

490 Racape V., Thierry Virginie, Mercier Herle, Cabanes Cecile (2019). ISOW spreading and mixing as revealed
491   by Deep-Argo floats launched in the Charlie Gibbs Fracture Zone . *Journal Of Geophysical*
492   *Research-oceans* , 124(10), 6787-6808 . https://doi.org/10.1029/2019JC015040

493 Roemmich, D., Alford, M. H., Claustre, H., Johnson, K. S., King, B., Moum, J., Oke, P. R., Owens, W. B., Pouliquen,
494   S., Purkey, S., Scanderbeg, M., Suga, T., Wijffels, S. E., Zilberman, N., Bakker, D., Baringer, M. O., Belbeoch,
495   M., Bittig, H. C., Boss, E., … Yasuda, I. (2019). On the future of Argo: A global, full-depth, multi-disciplinary
496   array. *Frontiers in Marine Science*, *6*(JUL), 1–28. https://doi.org/10.3389/fmars.2019.00439

497 Sallée, J. B., Pellichero, V., Akhoudas, C., Pauthenet, E., Vignes, L., Schmidtko, S., Garabato, A. N., Sutherland, P., &
498   Kuusela, M. (2021). Summertime increases in upper-ocean stratification and mixed-layer depth. *Nature*,
499   *591*(7851), 592–598. https://doi.org/10.1038/s41586-021-03303-x

500 Schmidtko, S., Stramma, L., & Visbeck, M. (2017). Decline in global oceanic oxygen content during the past five
501   decades. *Nature*, *542*(7641), 335–339. https://doi.org/10.1038/nature21399

502 Sharp, J. D., Fassbender, A. J., Carter, B. R., Johnson, G. C., Schultz, C., and Dunne, J. P.: GOBAI-O$_2$: temporally and
503   spatially resolved fields of ocean interior dissolved oxygen over nearly 2 decades, Earth Syst. Sci. Data, 15,
504   4481–4518, https://doi.org/10.5194/essd-15-4481-2023, 2023.

505 Stendardo, I., & Gruber, N. (2012). Oxygen trends over five decades in the North Atlantic. *Journal of Geophysical*
506   *Research: Oceans*, *117*(11), 1–18. https://doi.org/10.1029/2012JC007909

507 Stramma, L., Brandt, P., Schafstall, J., Schott, F., Fischer, J., & Körtzinger, A. (2008). Oxygen minimum zone in the
508   North Atlantic south and east of the Cape Verde Islands. *Journal of Geophysical Research: Oceans*, *113*(4), 1–15.
509   https://doi.org/10.1029/2007JC004369

510 Stramma, L., Prince, E. D., Schmidtko, S., Luo, J., Hoolihan, J. P., Visbeck, M., Wallace, D. W. R., Brandt, P., &
511   Körtzinger, A. (2012). Expansion of oxygen minimum zones may reduce available habitat for tropical pelagic
512   fishes. *Nature Climate Change*, *2*(1), 33–37. https://doi.org/10.1038/nclimate1304

513 Stramma, L., Schmidtko, S., Bograd, S. J., Ono, T., Ross, T., Sasano, D., & Whitney, F. A. (2020). Trends and decadal
514   oscillations of oxygen and nutrients at 50 to 300 m depth in the equatorial and North Pacific. *Biogeosciences*,
515   *17*(3), 813-831.

516 Stramma, L., Sunke Schmidtko (2021) Spatial and Temporal Variability of Oceanic Oxygen Changes and Underlying
517   Trends, Atmosphere-Ocean, 59:2, 122-132, DOI: 10.1080/07055900.2021.1905601

518 Thierry Virginie, Bittig Henry, The Argo-Bgc Team (2021). Argo quality control manual for dissolved oxygen
519   concentration. https://doi.org/10.13155/46542

520 Thierry Virginie, Bittig Henry, Gilbert Denis, Kobayashi Taiyo, Kanako Sato, Schmid Claudia (2022). Processing Argo
521   oxygen data at the DAC level. https://doi.org/10.13155/39795

522 Tjiputra, J. F., Goris, N., Lauvset, S. K., Heinze, C., Olsen, A., Schwinger, J., & Steinfeldt, R. (2018). Mechanisms and
523   Early Detections of Multidecadal Oxygen Changes in the Interior Subpolar North Atlantic. *Geophysical Research*
524   *Letters*, *45*(9), 4218–4229. https://doi.org/10.1029/2018GL077096

525 Yamaguchi, R., & Suga, T. (2019). Trend and Variability in Global Upper-Ocean Stratification Since the 1960s. *Journal*

526 *of Geophysical Research: Oceans, 124*(12), 8933–8948. https://doi.org/10.1029/2019JC01543

527 **Figures**

528
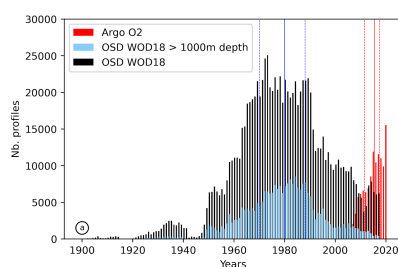
529
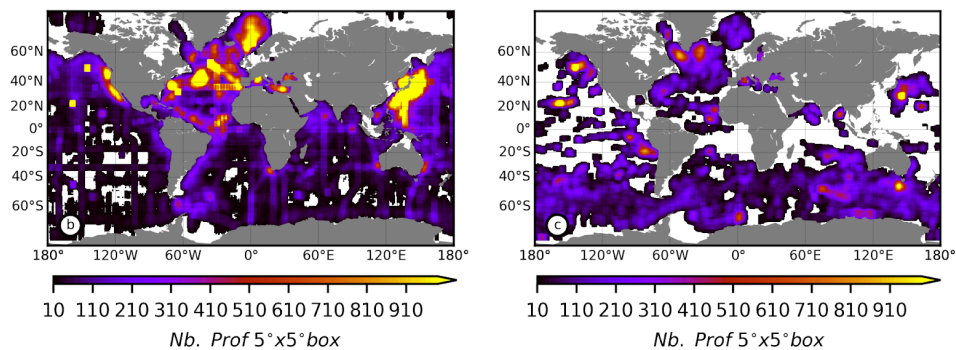
530

531 Figure 1 : a) Yearly distribution of DO profiles from WOD18 OSD used in WOA18 (black), WOD18 OSD profiles

532 deeper than 1000 m depth (blue), and DMQC Argo dataset used in ISASO2 (red) over the period 1899-2019. Solid lines

533 (dashed line) is the median (the first and third quartile) of the distribution. b) Density of DO OSD WOD18 profiles. c)

534 Density of DO Argo profiles.

23
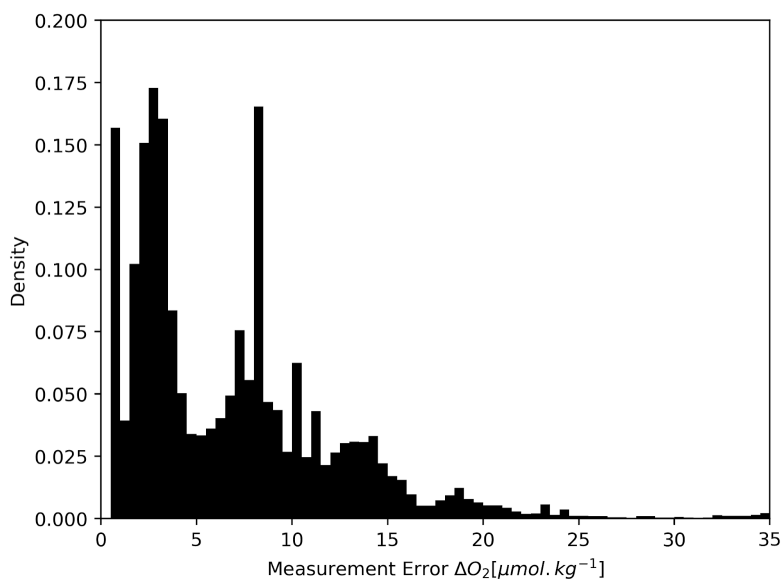
535

536 Figure 2: Distribution of the measurement error (DOXY_ADJUSTED_ERROR) from DO Argo S-profiles interpolated

537 on the ISAS standard z-levels.

538
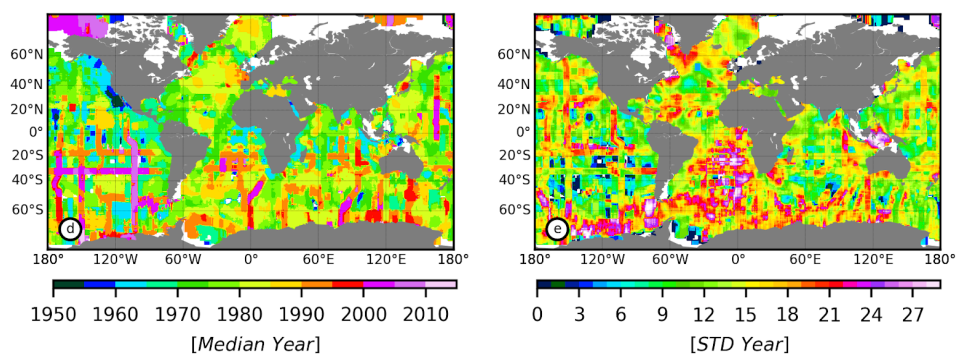
Figure 3 :d) Median year of sampling for DO OSD WOD18 profiles, and e) Standard deviation (in year) of the time

distribution for DO OSD WOD18 profiles, reaching at least 1000 m depth (in 5°x5° box).

25
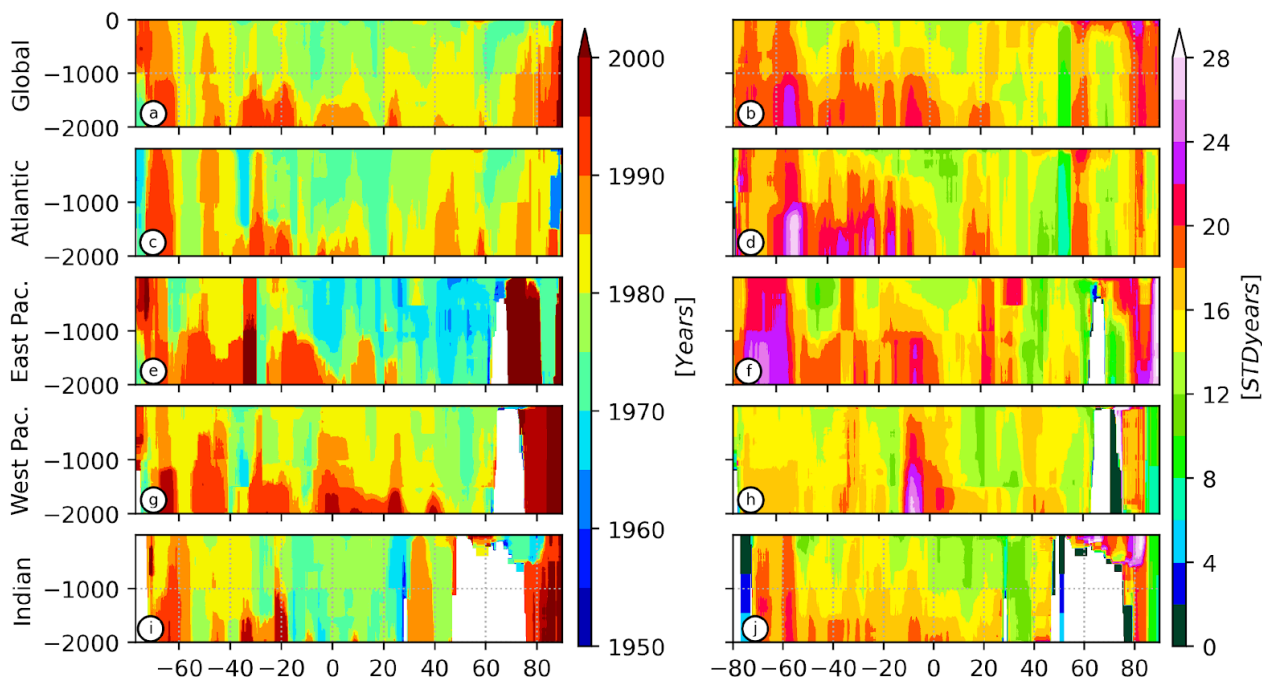
Figure 4: Meridional section of median time (left column) and STD (right column) for WOD18 OSD O2 profiles for a,b) global ocean ; c,d) Atlantic basin (90°W-20°E) ; e,f) Eastern Pacific (180°W-90°W) ; g,h) Western Pacific (120°E-180°E) and i,j) Indian (20°E-120°E). These time estimates are used to compute the equivalent trend for the difference between WOA18 and ISAS_MEAN sections.

547

548
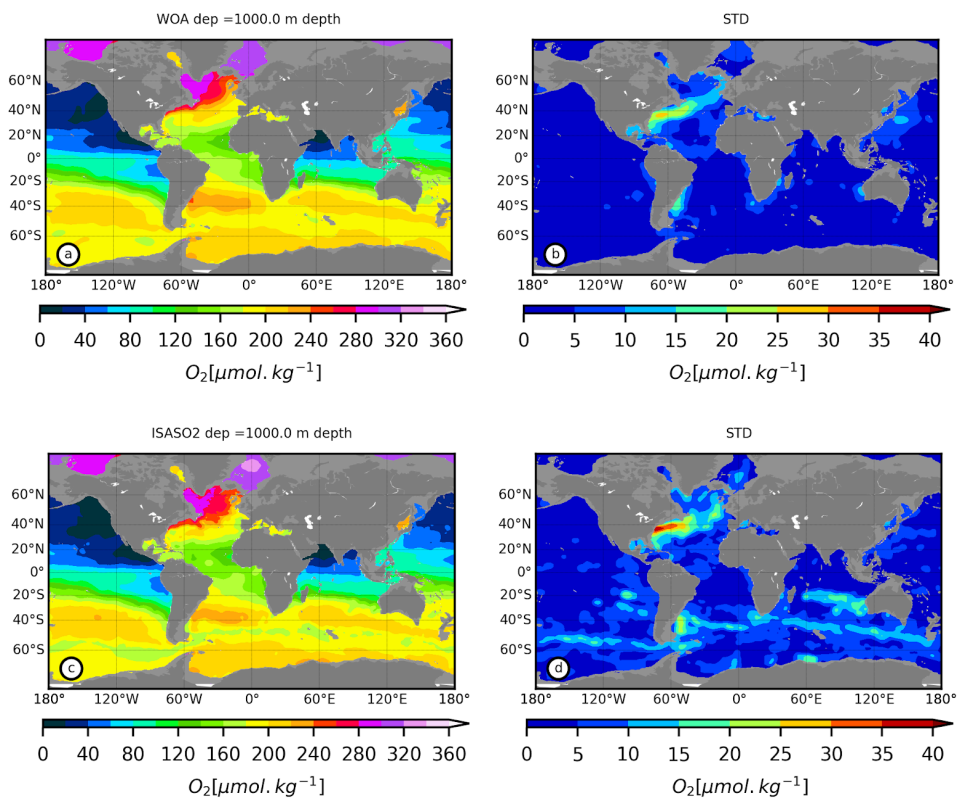
Figure 5: a) WOAO2 climatology of DO (in µmol.kg^{-1}) at 1000 m depth. b) WOAO2 climatology of STD (in µmol.kg^{-1})

between 2005-2019 at 1000 m depth. c) ISASO2 climatology of DO (in µmol.kg^{-1}) between 2005-2019 at 1000 m depth. d)

ISASO2 climatology of STD (in µmol.kg^{-1}) between 2005-2019 at 1000 m depth.

552
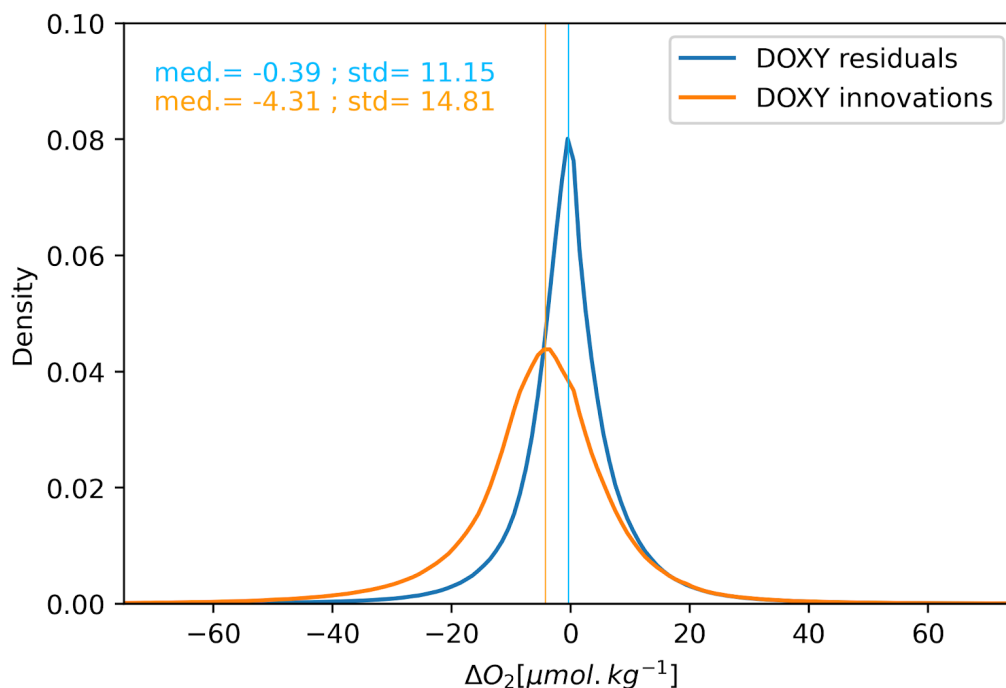
Figure 6: Density of residual distribution, i.e. difference between Argo data and ISAS_CLIM (blue) ; and innovation, i.e. difference between Argo data and first guess WOA18 (orange). The median for innovation is -4.31 µmol.kg^{-1}, suggesting a general deoxygenated bias between the WOA18 and Argo data likely due to i) a mean deoxygenation at the location of the DO Argo profile, or ii) remaining low oxygen bias in DO Argo profile. The median for residual is -0.39 µmol.kg^{-1}, suggesting that ISAS_CLIM estimates are slightly more oxygenated than DO Argo data at the location of the DO Argo profiles. This is likely due to the relaxation of the DO estimates toward the first guess (WOA18) and the smoothing in the OI procedure.
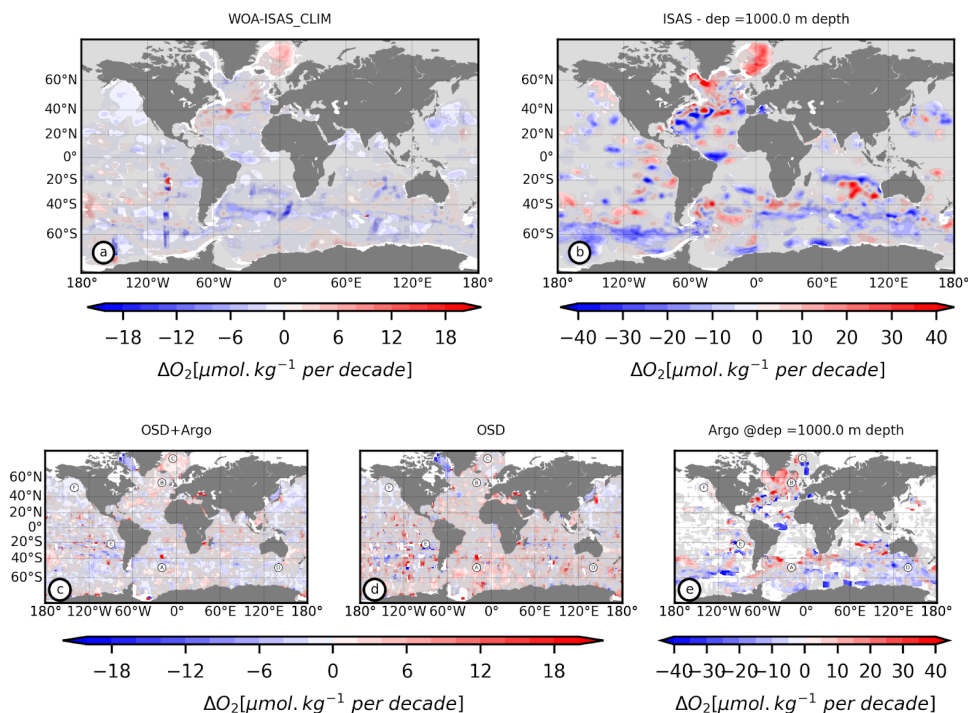
Figure 7: DO trend (in µmol.kg⁻¹ per decade) at 1000 m depth computed from a) difference between ISASO2_MEAN climatology minus WOA18 climatology, b) difference of the pendatal climatology (ISAS_M16 minus ISAS_M11); and the DO trend at 1000 m depth computed from individual DO profiles in 5°x5° boxes using c) OSD WOD18 + Argo data ; d) OSD WOD18 dataset alone ; and e) Argo DO dataset alone (2005-2020). Letter A-F on the cde) maps indicates the location of times series shown in Figure 8.
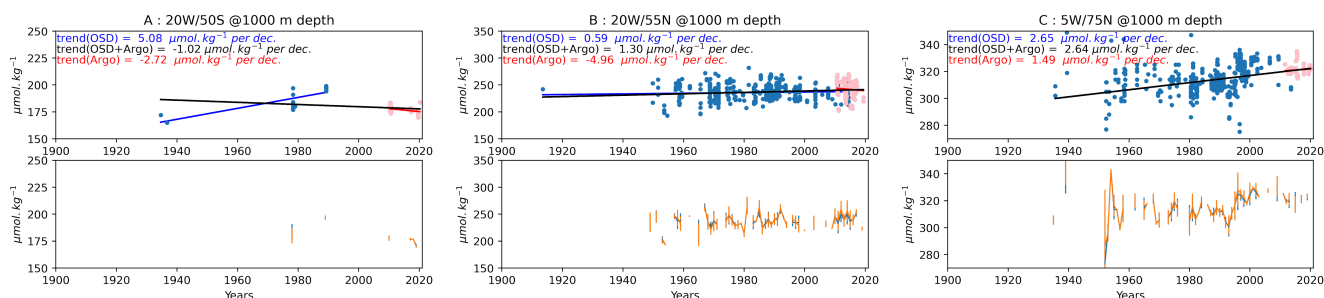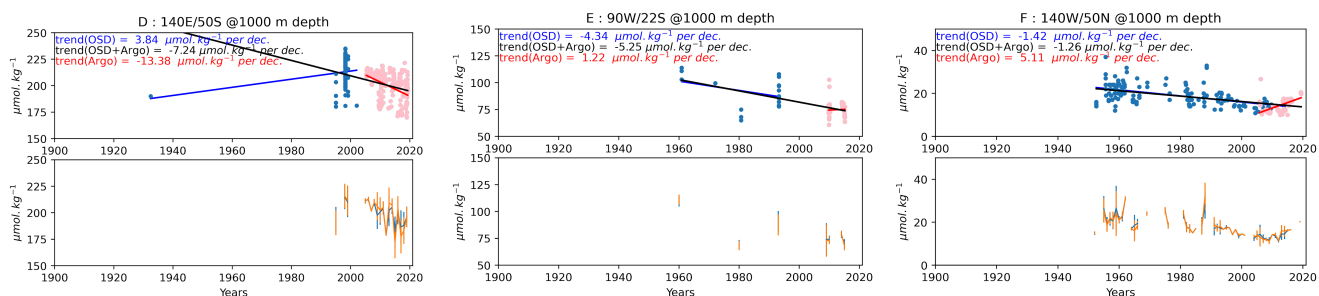
Figure 8: For each sub-panel: (upper sub-panel) DO trend computed in 5°x5° box at 1000 m depth for OSD WOD18 + Argo (black) data ; OSD WOD18 dataset alone (blue) ; and Argo DO dataset alone (2005-2020) (red). (lower sub-panel) : Time series of yearly mean (blue) and median (orange) and associated STD using OSD WOD18 + Argo dataset. Each 5°x5° box (see corresponding label on Fig. 7cbd) are centered on A : 20°W-50°S ; B : 20°W-55°N ; C : 5°W-75°N ; D : 20°W-140°E ; E : 90°W-22°S and F : 140°W-50°N.

579
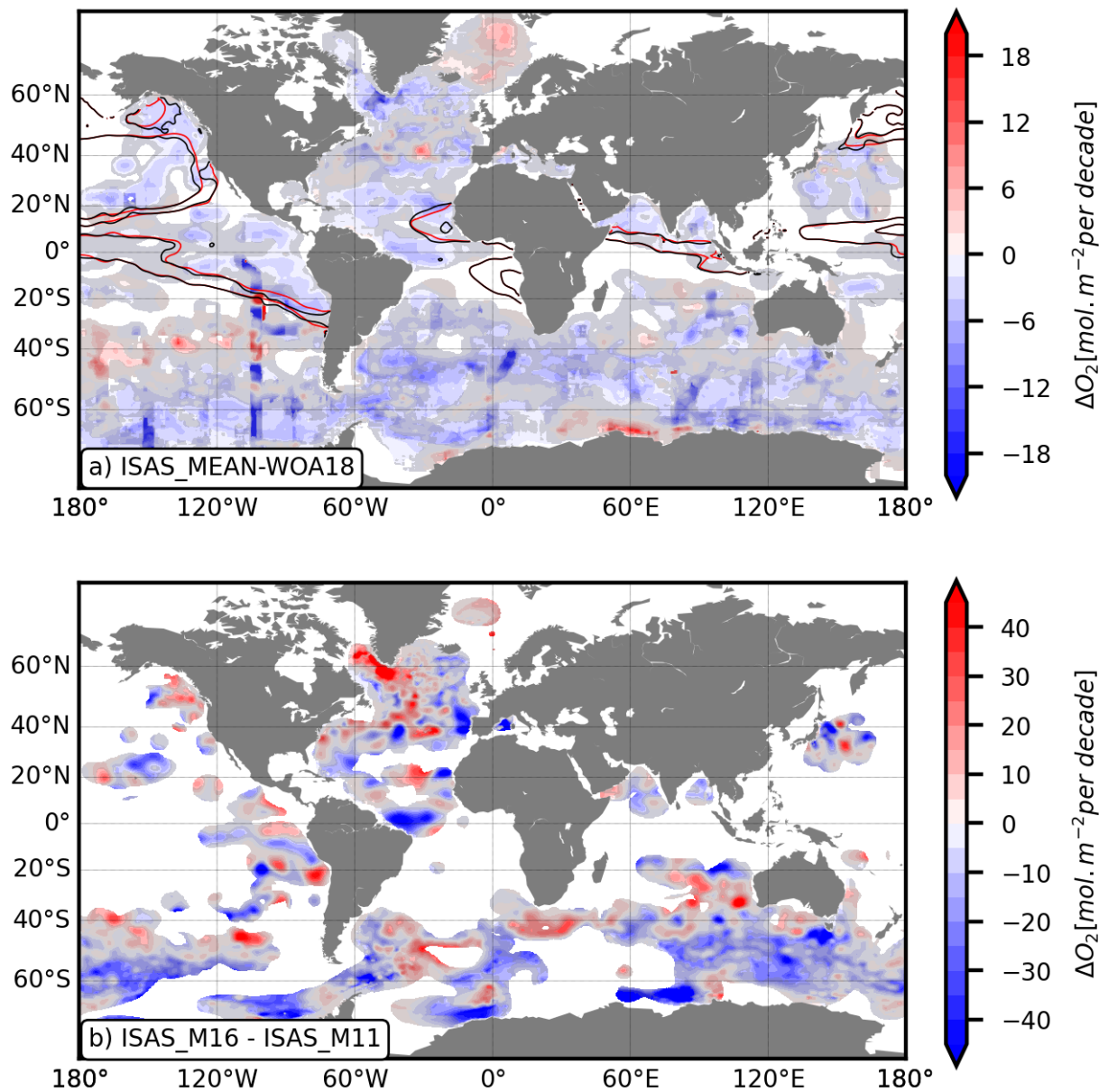
Figure 9: a) WOA18-ISASO2_MEAN equivalent trends (mol.m^{-2} per decade). Solid black (red) line are the WOA18 (ISASO2_MEAN) 40 and 80 µmol.kg^{-1} contours. b) ISASO2_M16-ISASO2_M11 equivalent trends (mol.m^{-2} per decade). Equivalent trends smaller than uncertainties are grey shaded, and PCTVAR larger than 95% are blanked in Fig. 2a and b.

31
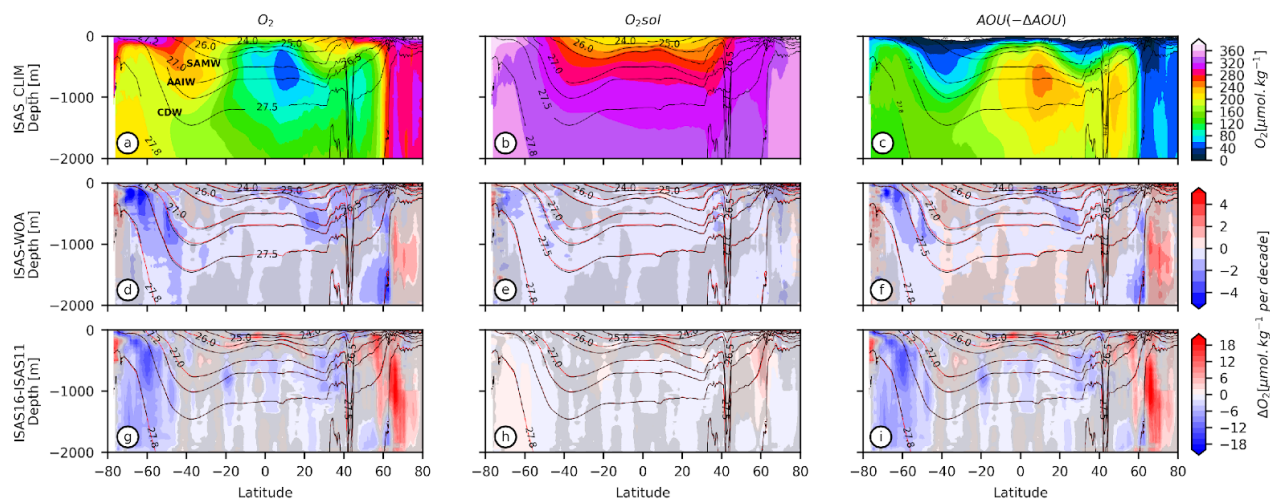
Figure 10: Global zonal average sections (ISASO2_MEAN), a) DO, b) Oxygen Saturation, c) Apparent Oxygen Utilization (AOU) (in µmol.kg⁻¹). ISASO2_CLIM-WOA18 d) DO difference, e) Oxygen Saturation anomaly, and f) -AOU anomaly. ISAS_M16-ISAS_M11 g) Dissolved Oxygen difference, h) Oxygen Saturation anomaly, and g) AOU anomaly. Black (red) contours correspond to the recent (older) climatological isopycnals (potential density in kg.m⁻³). Shading indicates when equivalent trends are smaller than uncertainties.
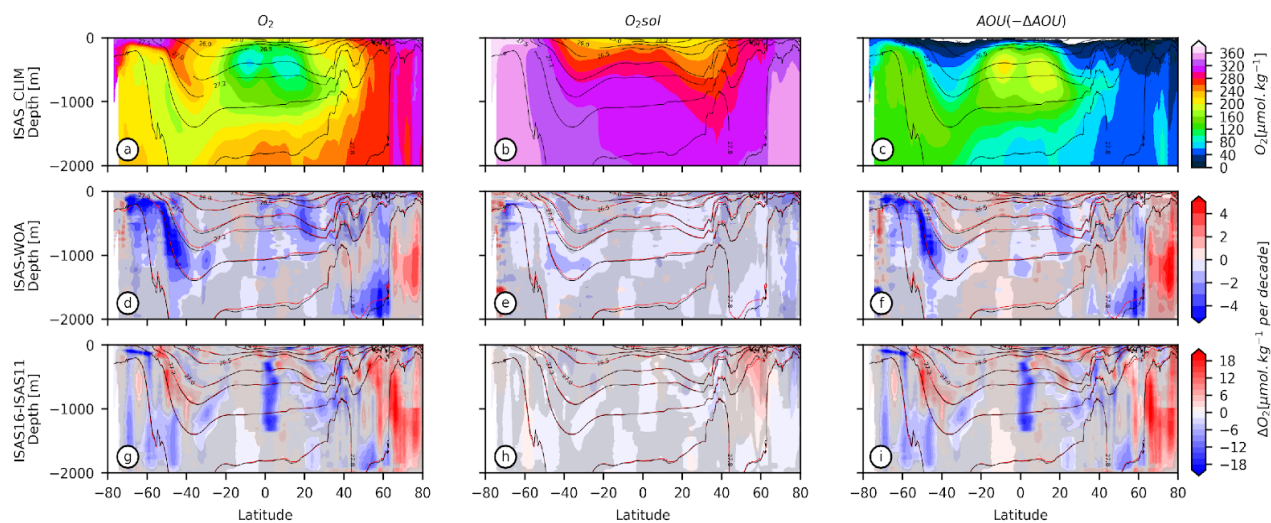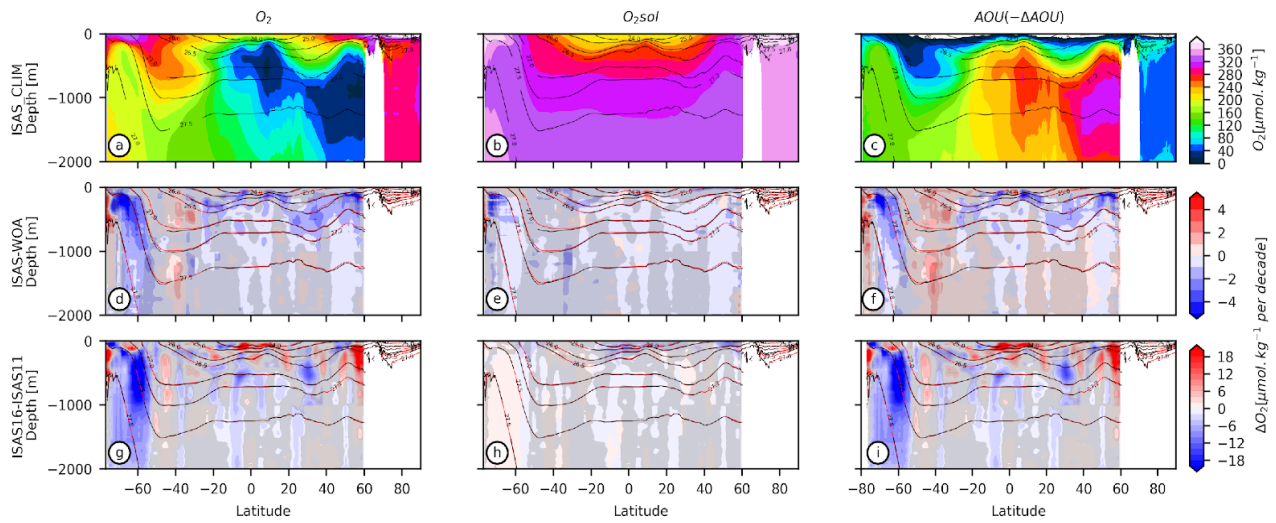
589

590 Figure 11: Same as Fig. 10 but for Atlantic basin only, averaged zonally (70°W-20°E).

591
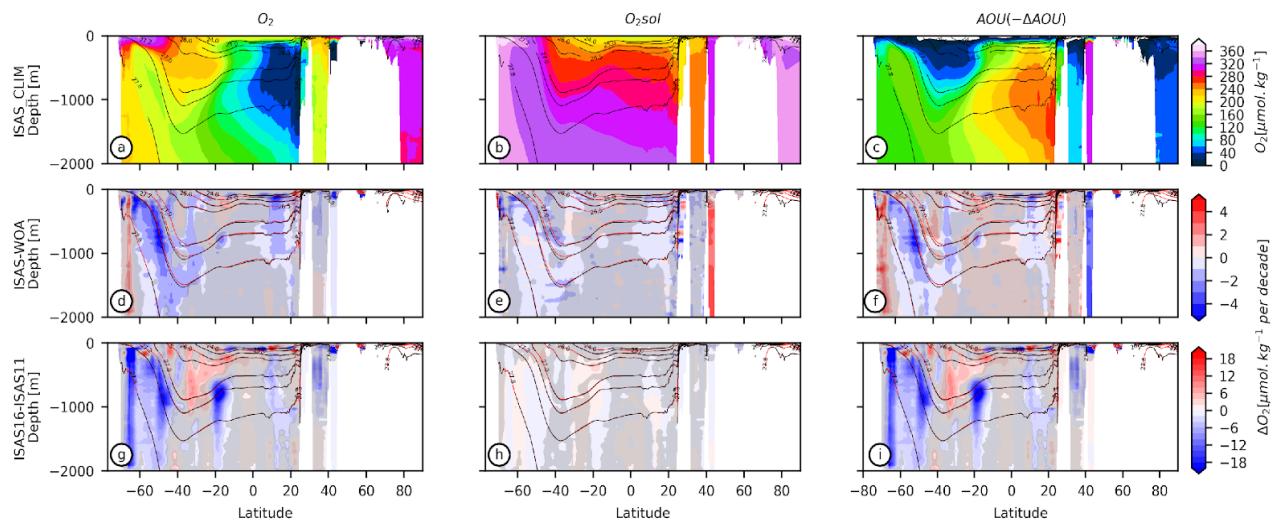
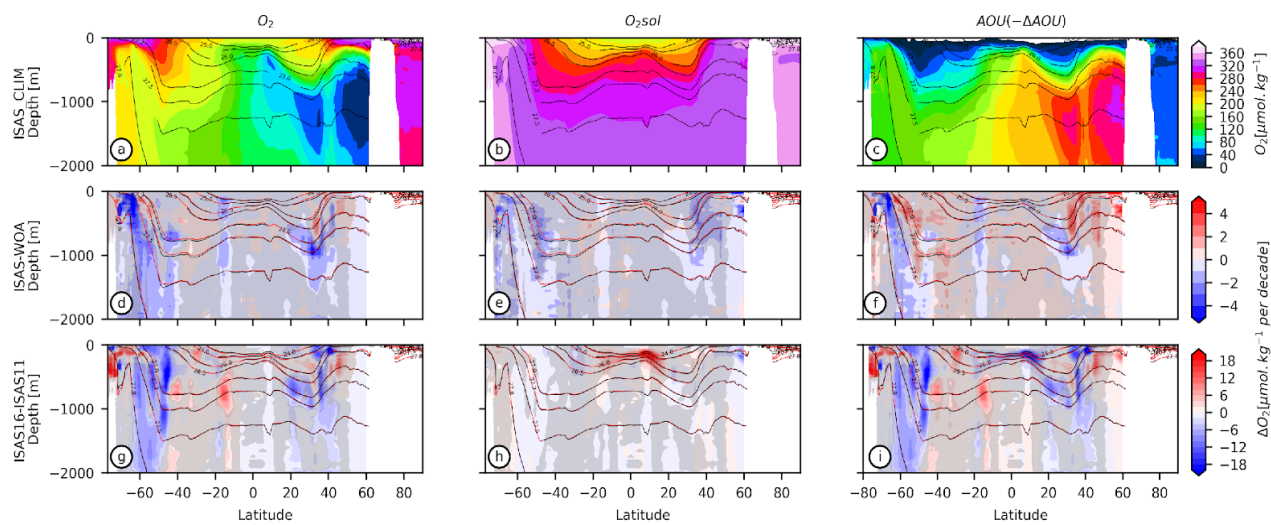Figure 12: Same as Fig. 10 but for the Indian basin only, averaged zonally (20°E-120°E).

593

594 Figure 13: Same as Fig. 10 but for the Eastern Pacific section averaged zonally (180°E-70°W).

595

Figure 14: Same as Fig. 103 but for the Western Pacific section averaged zonally (120°E-180°E).